CHAPTER IV
PVDF/ANTIMONY MODIFIED TITANIUM DIOXIDE ($Sb\text{-}TiO_2$) MEMBRANE FOR PEMFC APPLICATIONS

4.1 Abstract

PVDF/5 mol% $Sb\text{-}TiO_2$ composite film was prepared by solvent casting. By adding 5 mol% $Sb\text{-}TiO_2$ ceramic powder into the polyvinylidene fluoride (PVDF) matrix, the membrane was aimed to increase the hydrophilicity and proton conductivity at high temperature. Antimony modified titanium dioxide ($Sb\text{-}TiO_2$) was prepared via sol-gel method. The anatase structure of calcined $Sb\text{-}TiO_2$ at 500 ^{o}C was investigated by XRD. The presence of antimony in titania provides higher porosity and higher specific surface area. The composite films of 10%, 20%, 30%, 40%, and 50% by weight ceramic were fabricated by solvent casting using DMF as a solvent. TGA thermograms indicated the higher thermal stability with higher ceramic content. The microstructure of the composite was observed using SEM. The impedance of composites at different contents of ceramic was measured as a function of frequency using Hewlett-Packard 4194A impedance/gain phase analyzer. With increasing 5 mol%$Sb\text{-}TiO_2$ contents, a percentage of water uptake and the proton conductivity were increased.

Keywords: PVDF/5 mol% $Sb\text{-}TiO_2$ composite; Proton exchange membrane fuel cell

4.2 Introduction

Nowadays, fuel cell is very interesting as power sources for electric vehicles, stationary applications, and portable electronics. Among the several kinds, proton exchange membrane fuel cell (PEMFC) is the most popular choice because of its potential high efficiency, low operating temperature and usage safety. An important part of PEMFC is the polymer membrane which works as an efficient

polymer electrolyte, *i.e.*, conduct by protons whereas hindering electronic transport and penetration of fuel [1, 2].

Generally, perfluorinated membrane, Nafion, is used in practical cells, showing good ionic conductivity and chemical stability. Despite these good qualities, perfluorinated membranes still have few disadvantages, such as high cost, unstable mechanical properties at temperatures above 100 °C, and conductive only when soaked in water, which limits fuel cell operating temperatures to 80 °C. The operation of fuel cells at higher temperature own many advantages such as lower heat exchangers, and easier to integrate with reformers. Consequently, the development of membranes which are mechanically and chemically stable at higher temperatures (above 100 °C) is very interesting for studying fuel cells [3, 4].

Polymer matrix composite providing various advantages such as low cost, lightweight, and easier to manufacture than other materials, is one of the choices to improve high-temperature performance. The membrane is made with organic polymers containing ceramic fillers. Inorganic materials can have high proton conductivity with hydrophilicity, good chemical and thermal stability, high porosity, and high specific surface areas. Organic materials can make membranes elastic and have good mechanical properties with hydrophobicity. Thus, the composite film is applicable at higher temperature and moderate water vapor pressures [5-7].

In 2005, Colomer [15] prepared nanoporous anatase ceramic membranes with a BET surface area of 121 m^2/g, an average pore diameter of 5.8 nm and a pore volume of 0.236 cm^3/g. Proton conductivity of the membranes was measured as a function of temperature and relative humidity, R.H. When anatase membranes are treated at pH 1.5, the proton conductivity increased in the whole range of temperature and R.H. from room temperature to 90 °C. The highest value of proton conductivity was found to be 0.015 S/cm at 90 °C and 81% R.H. The similar values of proton conductivity, lower cost and higher hydrophilicity of these membranes make them potential substitutes for perfluorosulfonic polymeric membranes in proton exchange membrane fuel cells (PEMFCs).

In Tanita's work [6], niobium-modified titania and antimony/niobium-modified titania ceramic were prepared via the sol-gel technique. Inorganic membranes were fabricated by using the spin-coating technique using epoxy resin as

a binder. The proton conductivity value of TiO_2/epoxy membrane was enhanced by doping niobium and antimony into TiO_2 matrix and all of the nano-composite films present good thermal and mechanical properties.

In this study, the 5 mol% Sb-TiO_2 was prepared based on the sol-gel method. The PVDF/5 mol% Sb-TiO_2 composite films were prepared using solvent casting. Microstructure and distribution of ceramic power were observed by SEM and EDX. Higher proton conductivity and higher a percentage of water uptake were observed in composite films at higher ceramic contents.

4.3 Experiment

4.3.1 Materials

Titanium (IV) butoxide, glacial acetic acid and methyl alcohol were purchased from Italmar. The Poly(vinylidene fluoride) (PVDF) pellets were given by Solvay ($^{\#}$1008). *N,N*-Dimetyl formamide (DMF) was purchased from Lab Scan. Antimony (V) chloride was purchased from S.M. Chemical.

4.3.2 PVDF Film Preparation

Poly(vinylidene fluoride) pellets manufactured from Solvay Company (Belgium) (Solef 1008) were used. The fabrications of PVDF film was the solution casting which PVDF pellets were dissolved in DMF solution. The viscous solution was then casted on glass substrate. After the solvent evaporation in a vacuum oven at 60°C for 3 hours, the precursor membranes were washed in distilled water and dried in vacuum to assure the elimination of the solvent.

4.3.3 Sol-gel Processing of Antimony-modified Titania ceramics

Titanium (IV) butoxide (Ti $(OC_4H_9)_4$) was dissolved in the mixture between methanol/acetic acid ratio at room temperature with continuous stirring. The ratio of methanol/acetic acid was 1:1. In a different beaker, antimony (V) chloride ($SbCl_5$) was dissolved in methanol and gradually mixed with TiO_2 sol. After that, the gel was calcined at temperature about 500 °C for 3 hours. Antimony-modified titania particles was grounded into powder. TiO_2 powder was also prepared as a reference. The ceramic powder was characterized using XRD, SEM, and EDX. The surface area and pore size distribution were also measured using Nitrogen sorption.

4.3.4 PVDF/ Antimony-modified Titania composite Preparation

PVDF powder supplied by Solvay (Solef 1008) was dissolved in dimethyl formamide (DMF) at 60°C. For composite preparation, the ratio of polymer and solvent was 1:10 w/v. Proportionate quantity of Antimony-modified Titania ceramics powder was added in the polymer solution. It was homogenized by magnetic stirrer. The solution was then cast on a glass substrate. After that, the solvent was evaporated at 60°C for 3 hour under vacuum. Following this method, the composite films of 10%, 20%, 30%, 40%, and 50% by weight ceramic were fabricated. The precursor membranes were washed with distilled water and dried in vacuum. The dispersion of ceramic particles was observed by using SEM and EDX-mapping. The composite membranes were tested in order to evaluate the potential use as electrolyte in PEMFCs at high temperature by using TGA, Impedance spectroscopy and Water uptake. Lloyd Universal Testing machine were carried out to measure the mechanical properties of the thin films.

4.3.5 Characterization

Crystal structure of ceramic was characterized by X-ray diffraction (Rigaku, model Dmax 2002). The specific surface area and the pore size distribution were measured by using Thermo Finnigan, Autosorb-1 from Quantachrome Company. The distribution of ceramic powders in composites was observed using a Hitachi/S-4800 field emission scanning electron microscope and the doped Sb species were identified by LINK ISIS series 300 for Energy dispersive X-ray (EDX) analysis. Thermal stabilities of composite film were investigated by Thermal gravimetric Analyzer, Perkin-Elmer TG-DTA pyres diamond. Mechanical properties of the thin films were investigated by using a Model LRX Lloyd Universal Testing machine following ASTM D882. The water uptake (%W) was measured by soaking the samples in the water. The impedance of the samples was measured by using impedance analyzer (Hewlett Packard., model 4194A) in impedance (Z) mode, with frequency from 1 kHz to 10 MHz.

4.4 Results and Discussion

4.4.1 Antimony Modified Titanium Dioxide (Sb-TiO_2) in Various Amounts of Antimony

4.4.1.1 XRD Analysis of Pure and Sb Doped TiO_2 Particles

The crystal structure of pure and Sb doped TiO_2 particles were examined by XRD. All of the samples were calcined at 500 °C for 3 h in a furnace and the diffractograms shown in Fig.4.1 indicate that all of the samples possess an anatase phase and no peaks of rutile and mixed phases were found.

Table 4.1 Summary of physical properties of TiO_2 and Sb doped TiO_2 samples

Sample	Crystal Size (nm)	2Θ Position of 1 0 1 Peak	$d_{(h\ k\ l)}$ (nm)	Lattice Parameter	
				a (Å)	*c* (Å)
TiO_2	14.64568	25.367	0.35083	3.776	9.486
5mol%Sb-TiO_2	11.50039	25.322	0.351443	3.783	9.497
10mol%Sb-TiO_2	11.2463	25.325	0.351402	3.7822	9.5023
20mol%Sb-TiO2	11.48518	25.367	0.35083	3.776	9.486

The anatase peaks were indexed as (101), (004), (200), (105), (211), (204), (116), (220) and (215) in the order of increasing diffraction angles, indicating a body centered tetragonal crystalline structure of TiO_2 crystal [9]. It also shows that the increase of the full width at half-maximum (FWHM) of the XRD peaks with doping antimony exhibits the decrease of grain size, as reported in Table 4.1.

The grain size of the TiO_2 and Sb-TiO_2 powders were calculated using the Scherrer equation [10]. It is worth noting that the crystal size of doped particles decreased by an introduction of Sb dopant into TiO_2 crystal [11].

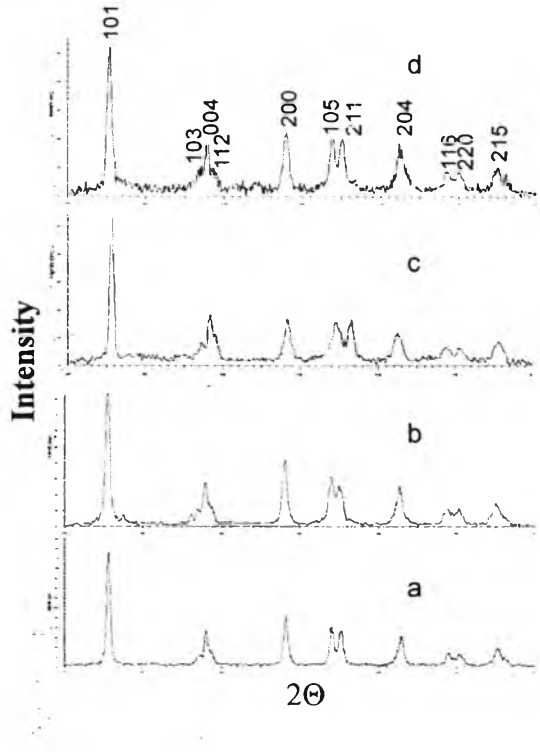

Figure 4.1 XRD patterns for (a) TiO_2, (b) 5 mol%Sb-TiO_2, (c) 10 mol%Sb-TiO_2, (d) 20 mol%Sb-TiO_2 which all of these were calcined at 500 ° C.

The doping of antimony atoms into the TiO_2 lattice did not give any significant changes in the diffractograms. The lattice parameters a and c, as listed in Table 4.1, were calculated based on Bragg's law ($2d \sin\theta = \lambda$) and a formula for a tetragonal system [12],

$$\frac{l}{d^2} = \frac{h^2 + k^2}{a^2} + \frac{l^2}{c^2}$$

There is no considerable difference in the lattice parameters of doped materials, this suggests that the structure of doped TiO_2 samples was not changed or distorted from anatase structure of pure TiO_2.

4.4.1.2 Surface Area and Pore Size Analysis of TiO_2 and Sb Doped TiO_2 Particles

The results from the surface area, pore size and pore volume measurement of TiO_2 after calcinations at 500 °C were summarized in Table 4.2. The materials present type IV of N_2 adsorption-desorption isotherms with hysteresis loops in Fig. 4.2, clearly indicating the mesoporous nature of TiO_2 and Sb doped TiO_2 samples. The volume adsorbed for all isotherms sharply increased at high relative pressure (P/P_0), representing capillary condensation of nitrogen within the irregular mesopore structure.

Table 4.2 Physicochemical properties of TiO_2 and Sb doped TiO_2 samples calcined at 500 °C

Samples	S_{BET} (m^2g^{-1})	D_{Pore} (nm)	V_{Pore} (cc g^{-1})
TiO_2	61.09	7.06	0.1078
5 mol% Sb-TiO_2	92.9	11.4	0.2647
10 mol% Sb-TiO2	93.48	16.09	0.2956
20 mol% Sb-TiO2	92.34	14.68	0.2655

As shown in Table 4.2, the surface area of Sb doped TiO_2 were higher than that of pure TiO_2. This increasing was due to the presence of Sb^{5+} on the surface of TiO_2 which inhibits densification and crystalline growth of TiO_2 nanoparticles by providing dissimilar boundaries [13].

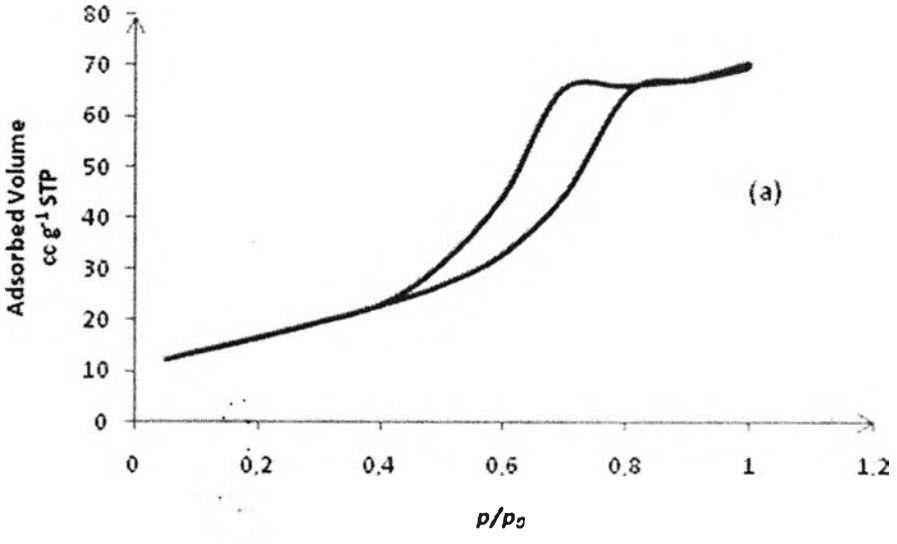
Adsorbed Volume
cc g-1 STP
80
70
60
50
40
30
20
10
0
0
0,2
0,4
0,6
0,8
1
1,2
p/p0
(a)

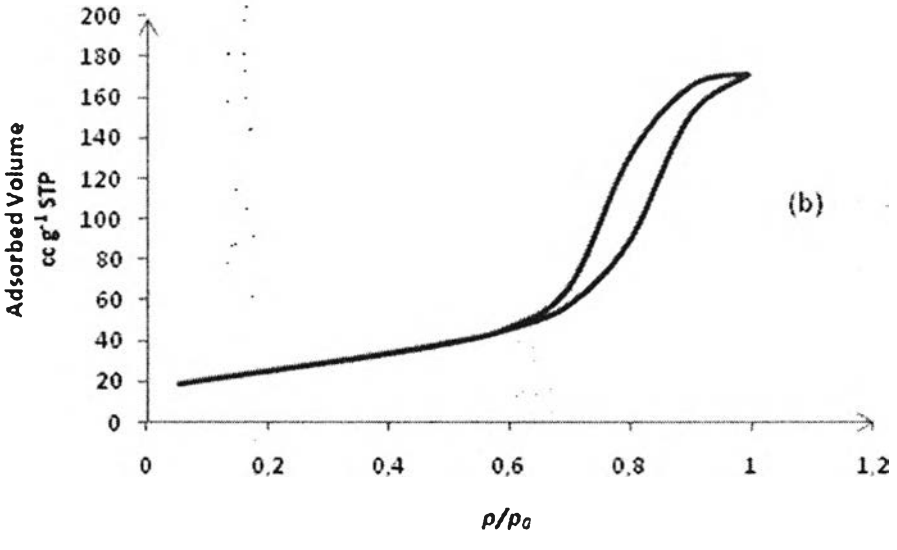
Adsorbed Volume
cc g-1 STP
200
180
160
140
120
100
80
60
40
20
0
0
0,2
0,4
0,6
0,8
1
1,2
p/p0
(b)

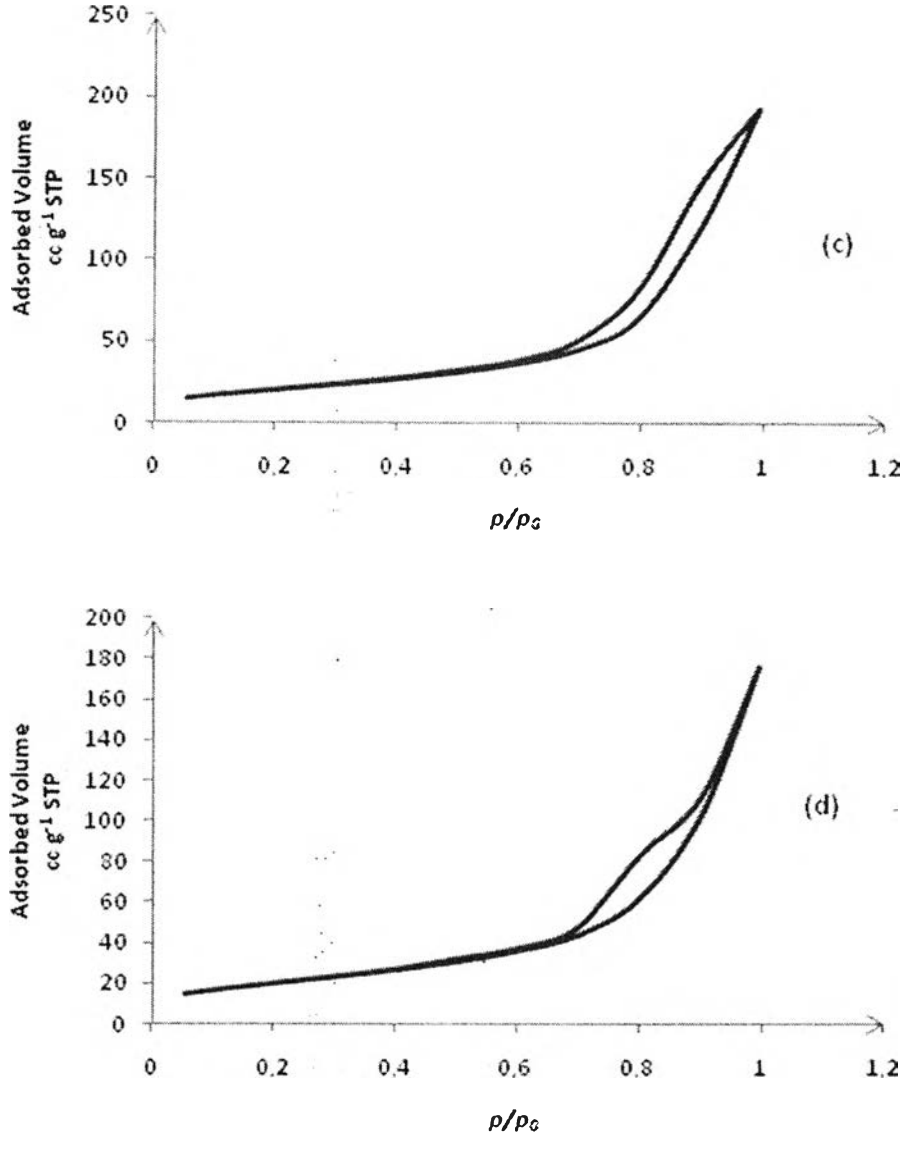

Figure 4.2 N_2 adsorption-desorption isoterms of (a) TiO_2, (b) 5 mol%Sb-TiO_2, (c) 10 mol%Sb-TiO_2, (d) 20 mol%Sb-TiO_2 samples calcined at 500 ° C.

4.4.1.3 SEM/EDX Analysis of TiO_2 and Sb Doped TiO_2 Particles

SEM photographs of particles obtained present spherical morphology of pure and doped TiO_2 nanoparicles and it was not significantly changed according to the introduction of Sb dopant as shown in Fig. 4.3.

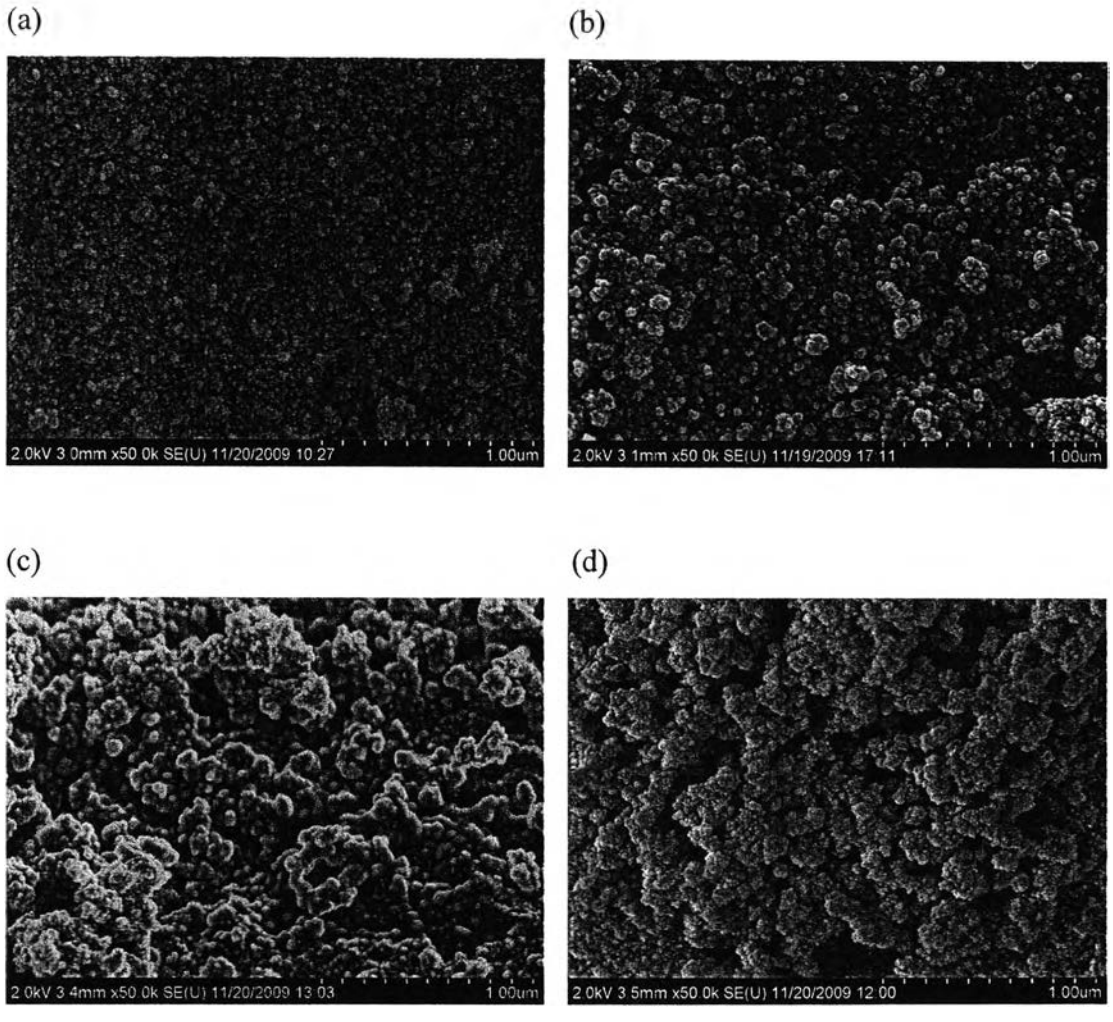

Figure 4.3 SEM images of (a) TiO_2, (b) 5 mol%Sb-TiO_2, (c) 10 mol%Sb-TiO_2, (d) 20 mol%Sb-TiO_2 samples calcined at 500 ° C.

In order to identify the presence of Sb^{5+} ions in the TiO_2 matrix, EDX spectrum was carried out. The EDX spectrum shown in Fig. 4.4 confirmed that most of Sb^{5+} ions incorporated into the framework of TiO_2 and substitute for the Ti^{4+} sites. Moreover, the results suggested that Sb was incorporated into the TiO_2 crystal because any peak corresponding to Sb-related compounds was not detected by X-ray diffraction patterns.

(a)

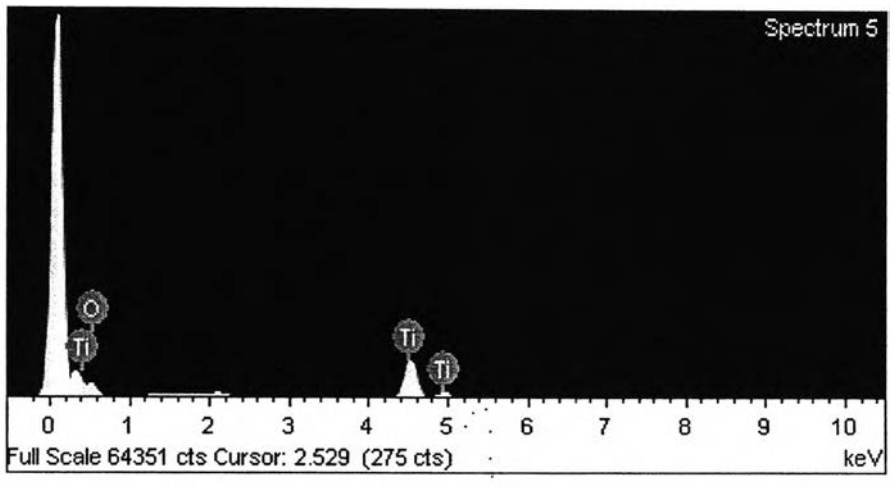
Spectrum 5
O
Ti
Ti
Ti
0 1 2 3 4 5 6 7 8 9 10
Full Scale 64351 cts Cursor: 2.529 (275 cts)
keV

(b)

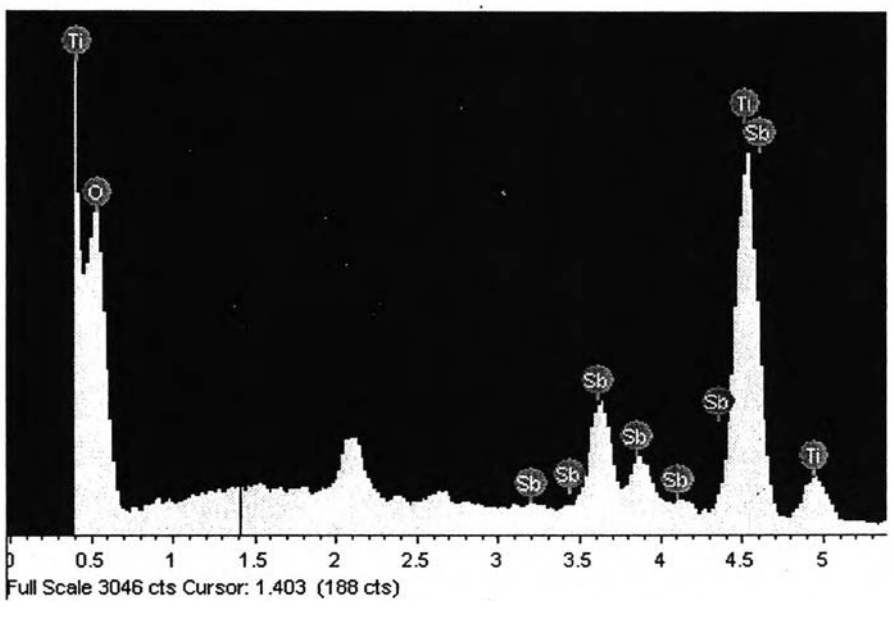
Ti
O
Ti
Sb
Sb
Sb
Sb
Sb
Sb
Sb
Ti
0 0.5 1 1.5 2 2.5 3 3.5 4 4.5 5
Full Scale 3046 cts Cursor: 1.403 (188 cts)

(c)

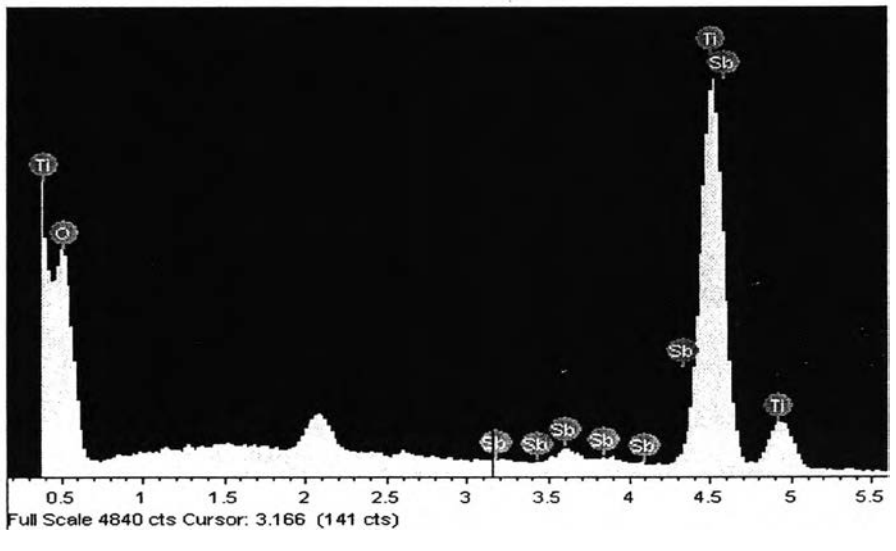
Ti
Sb
Ti
O
Sb
Ti
Sb
Sb
Sb
Sb
Sb
0.5 1 1.5 2 2.5 3 3.5 4 4.5 5 5.5
Full Scale 4840 cts Cursor: 3.166 (141 cts)

(d)

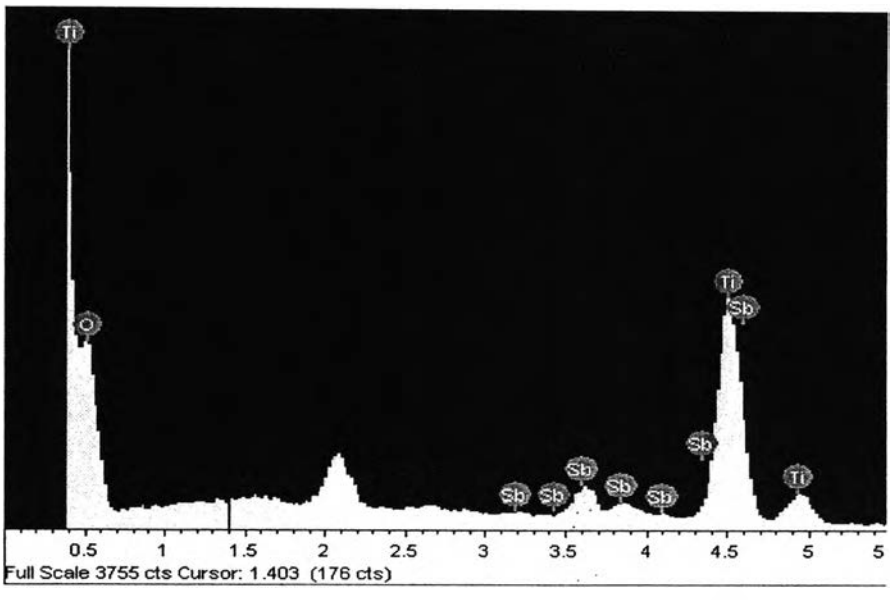

Figure 4.4 EDX graphs of (a) TiO_2, (b) 5 mol%Sb-TiO_2, (c) 10 mol%Sb-TiO_2, (d) 20 mol%Sb-TiO_2 samples calcined at 500 ° C.

4.4.2 PVDF-10%wt of Antimony Modified Titanium Dioxide (Sb-TiO_2) Composite Film at Various Amounts of Antimony

4.4.2.1 SEM/EDX Analysis of PVDF-10%wt of Sb Doped TiO_2 Films

SEM micrograph of the composites containing 10%wt of Sb doped TiO_2 filler in various amounts of Sb which fine powder was dispersed in a PVDF matrix were shown in Figures 4.5.

(a) (b)

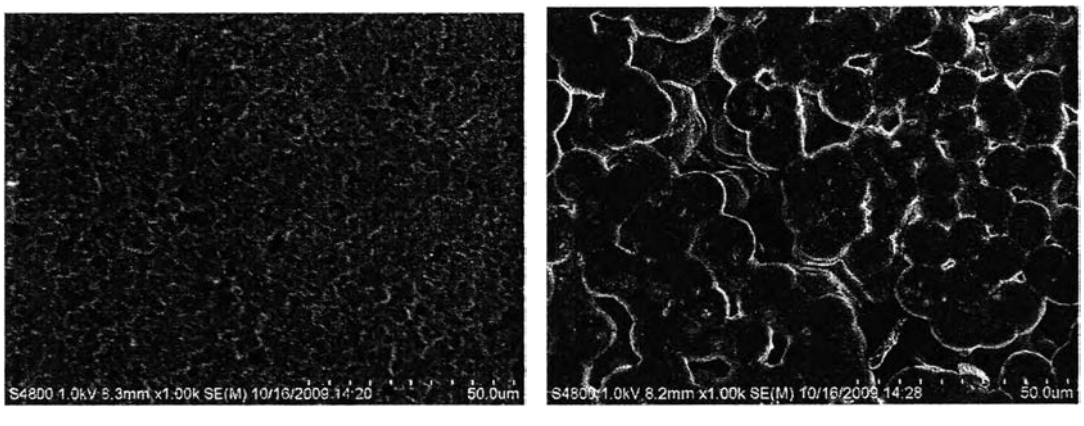

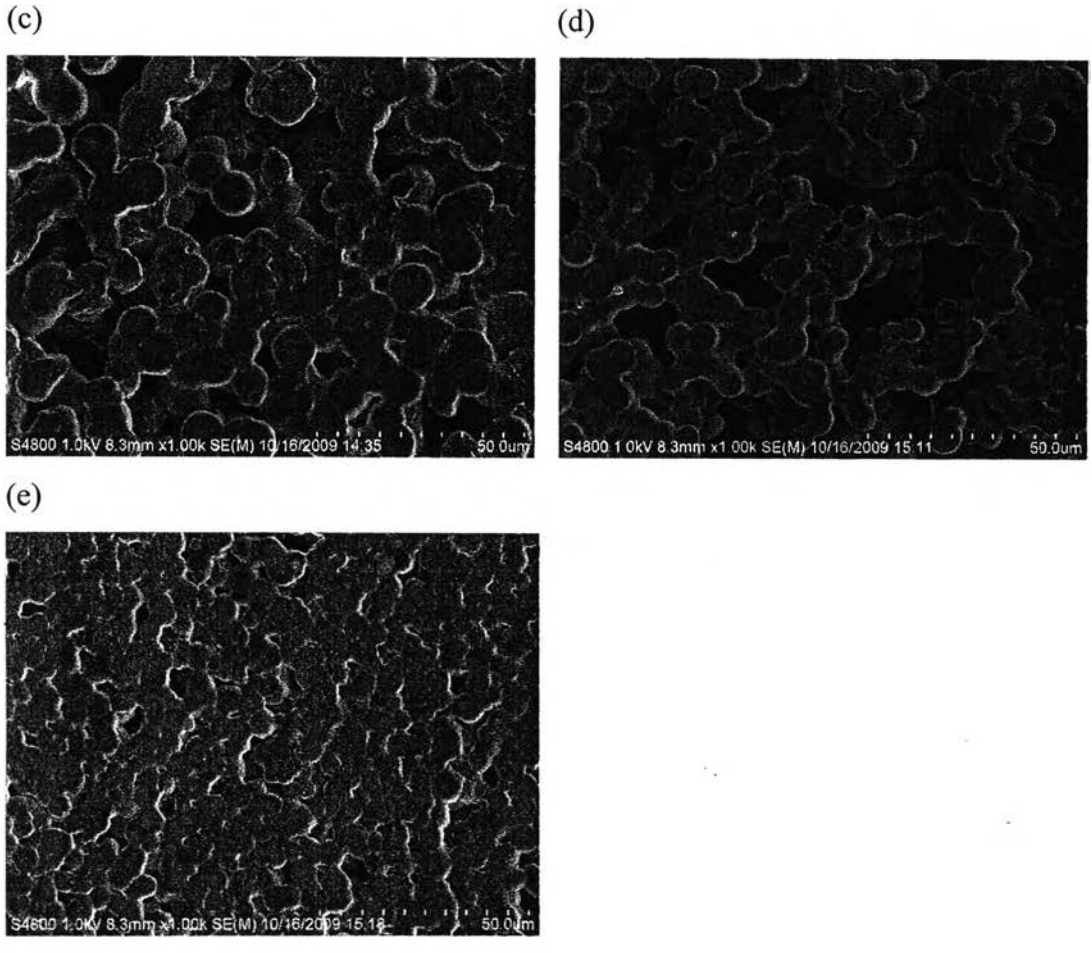

Figure 4.5 SEM images of (a) PVDF cast film, (b) PVDF-10%wt of TiO_2, (c) PVDF-10%wt of 5 mol%Sb-TiO_2, (d) PVDF-10%wt of 10 mol%Sb-TiO_2, (e) PVDF-10%wt of 20 mol%Sb-TiO_2.

In addition, EDX analysis was used to observe the distribution and dispersion of ceramic powder in the PVDF matrix. EDX Sb and Ti-mapping photographs show the homogeneous and uniform distribution of Sb-TiO_2 ceramic in PVDF matrix as presented in Fig. 4.6, 4.7, 4.8 and 4.9.

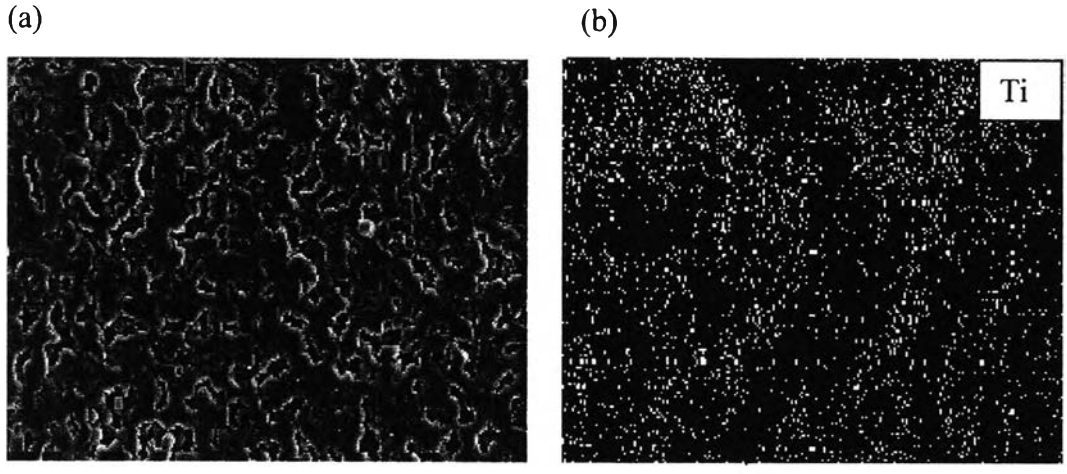

Figure 4.6 (a) SEM image (scale bar = 10 μm), (b) EDX Ti-mapping photograph of PVDF-10%wt of TiO_2.

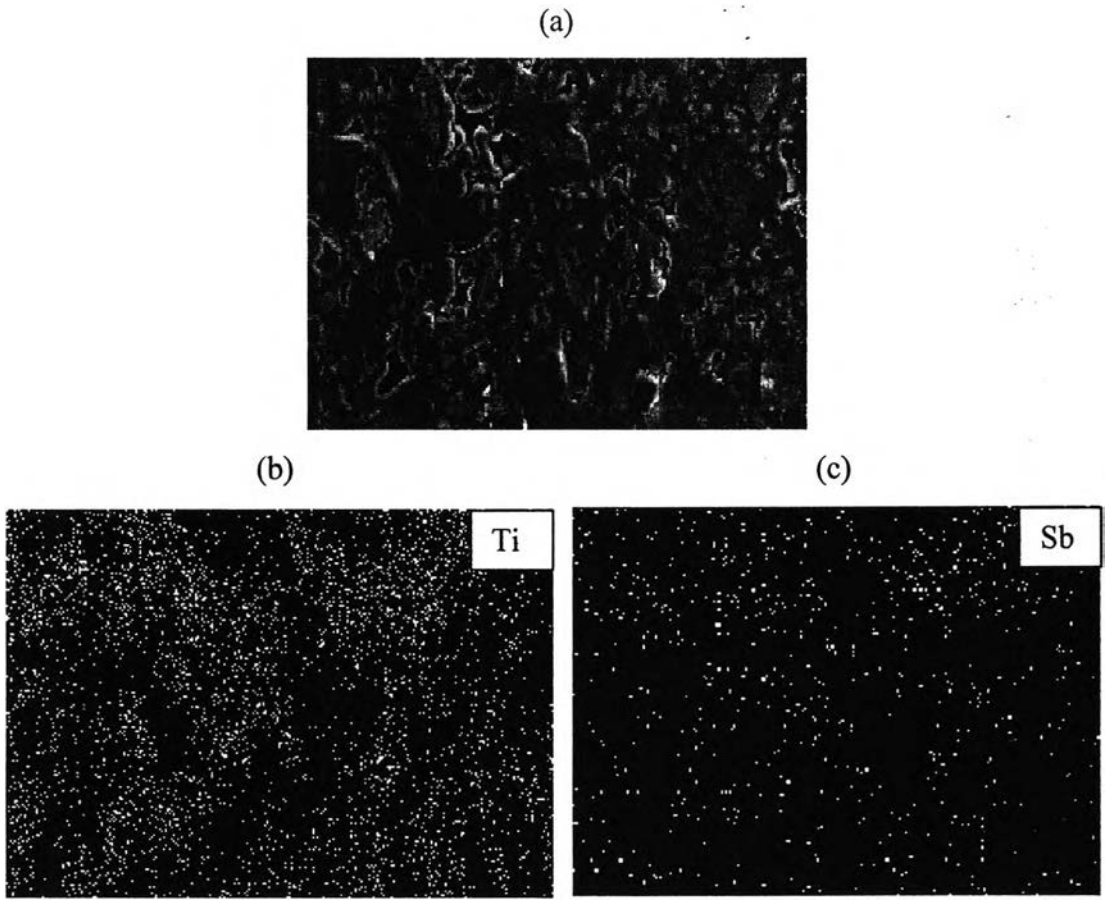

Figure 4.7 (a) SEM image (scale bar = 10 μm), (b) EDX Ti-mapping photograph, (c) EDX Sb-mapping photograph of PVDF-10%wt of 5 mol%Sb-TiO_2.

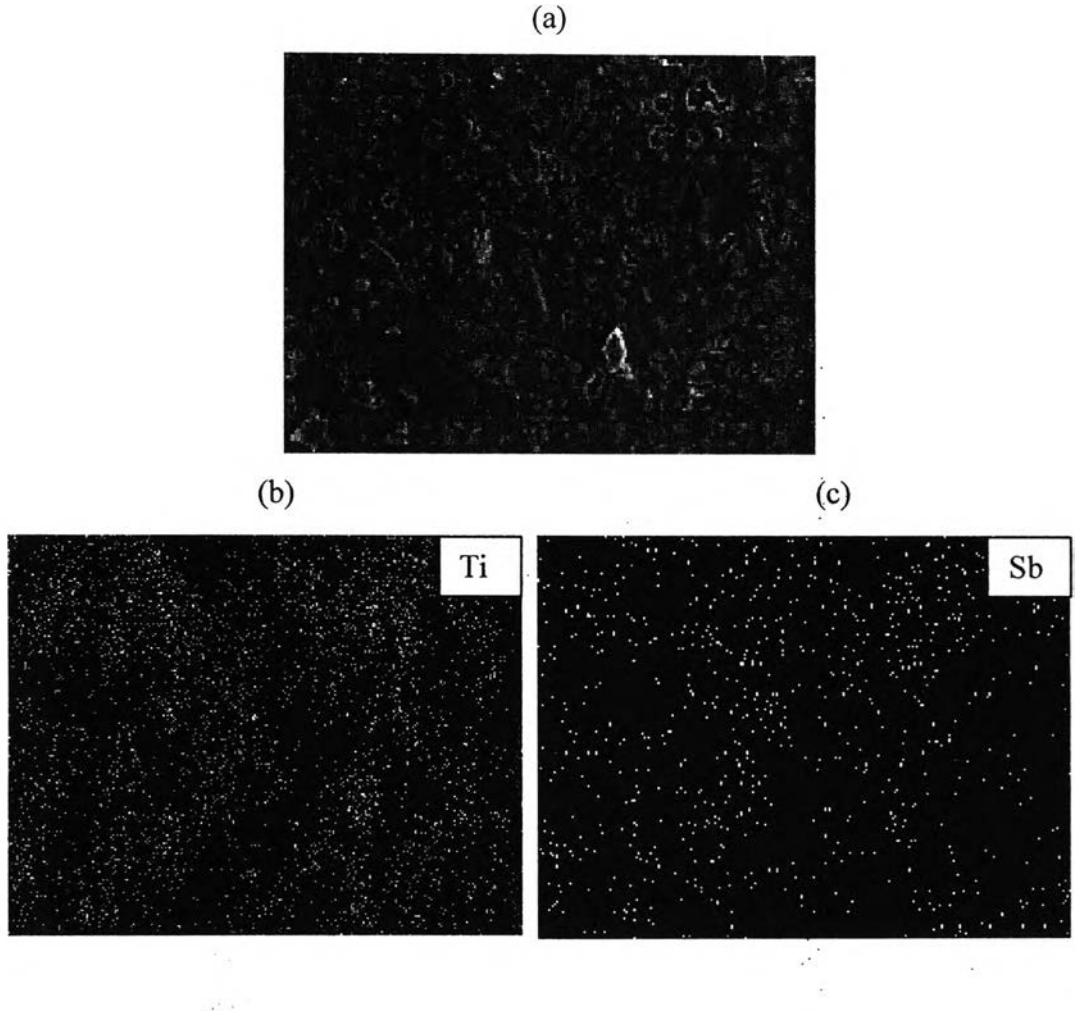

Figure 4.8 (a) SEM image (scale bar = 10 μm), (b) EDX Ti-mapping photograph, (c) EDX Sb-mapping photograph of PVDF-10%wt of 10 mol%Sb-TiO_2.

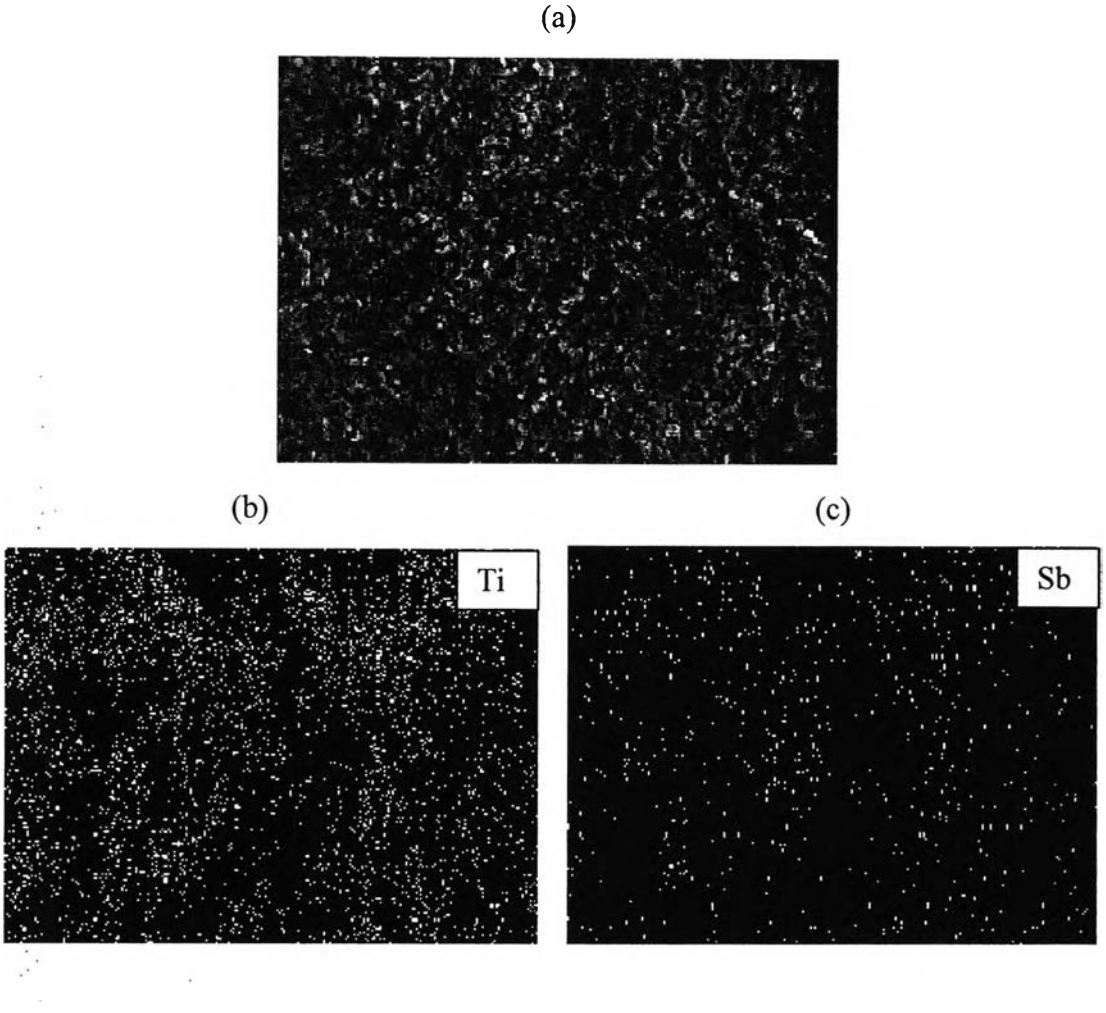

Figure 4.9 (a) SEM image (scale bar = 10 μm), (b) EDX Ti-mapping photograph, (c) EDX Sb-mapping photograph of PVDF-10%wt of 20 mol%Sb-TiO_2.

4.4.2.2 TGA Analysis of PVDF-10%wt of Sb Doped TiO_2 Cast Films

The hydration effect and thermal stability of thin films were also examined using TGA analysis. As shown in Fig.4.10, the mass loss for all of the samples occurs in 2 steps in a wide temperature range from room temperature to 900 °C. It can be observed that the relative mass decayed at temperature below 150 °C and another mass loss is at approximately near 400 °C. The first mass loss indicates the presence of water, while the second one presents the decomposition of PVDF. Moreover, there was no significant shift of TGA thermographs among PVDF/Sb-TiO_2 thin films. Therefore, this suggested that the amounts of Sb dopant does not influence the degradation of thin films.

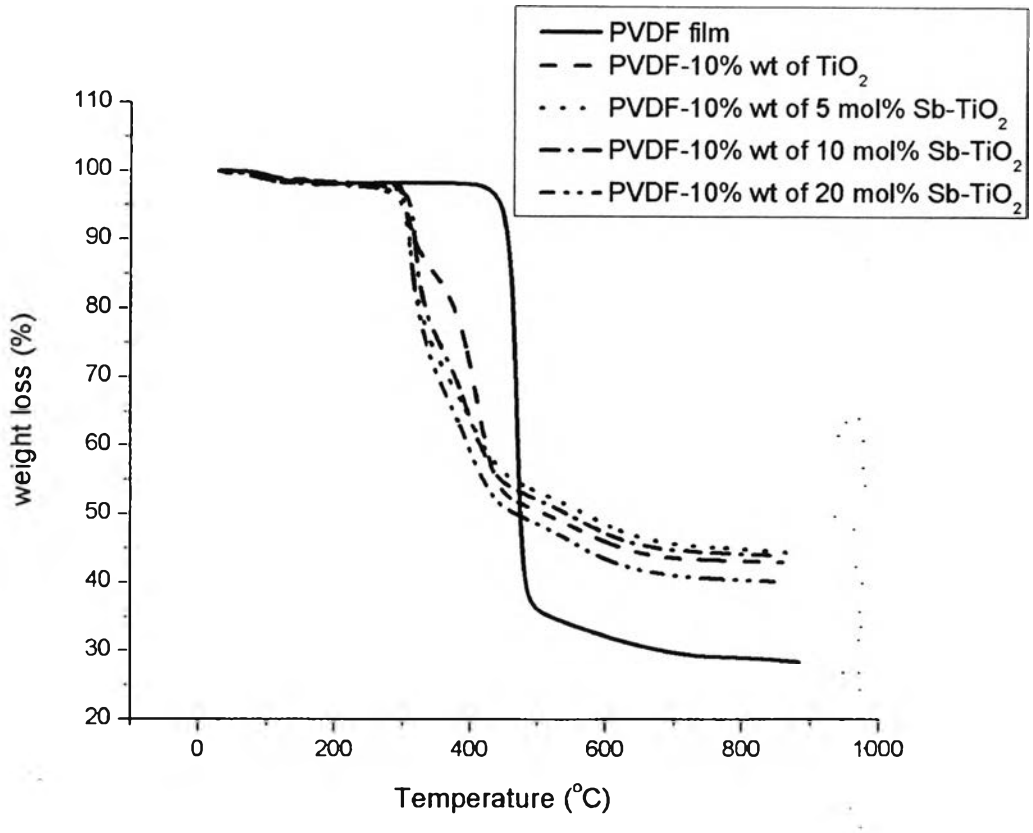

Figure 4.10 TGA thermograms of PVDF cast film and PVDF-10%wt of Sb doped TiO_2 cast films.

4.4.2.3 Mechanical Properties of PVDF-10%wt of Sb Doped TiO_2 Cast Films

Tensile properties were measured in order to evaluate the stiffness and strength of the thin films. As it can be seen in the Table 4.3, the PVDF/10%wt of Sb doped TiO_2 cast films have Young's Modulus better than that of PVDF film. This may be contributed the high modulus of ceramic. On the other hand, the percentage strain at break and the stress at break of PVDF film are better than those of composite films because the chain flexibility of the polymer in composite was restricted [14] and the interfacial interaction between polymer and ceramic was weak.

Table 4.3 Mechanical properties of PVDF cast film and PVDF/10%wt of Sb doped TiO_2 cast films

Samples	Young's Modulus (MPa)	Stress at Break (MPa)	Percentage Strain at Break
PVDF Cast Film	272.42 ± 2.45	24.66 ± 3.38	17.00 ± 1.26
PVDF/10%wt of TiO_2	395.26 ± 3.58	16.59 ± 2.41	13.58 ± 2.55
PVDF/10%wt of 5 mol%Sb-TiO_2	432.02 ± 3.35	17.17 ± 3.78	12.75 ± 3.05
PVDF/10%wt of 10 mol%Sb-TiO_2	383.19 ± 4.14	16.80 ± 4.56	13.08 ± 2.61
PVDF/10%wt of 20 mol%Sb-TiO_2	408.32 ± 2.96	16.73 ± 2.74	11.87 ± 2.84

4.4.2.4 Water Uptake Testing of PVDF-10%wt of Sb Doped TiO_2 Cast Films

The results of water uptake testing at room temperature exhibit that composite films have higher percentage of water uptake than PVDF film because of the hydrophilicity of the ceramics and the PVDF/Sb doped TiO_2 films possess higher percentage of water uptake than PVDF/TiO_2 film, as shown in Table 4.4. This increase may be due to the higher specific surface areas of doped TiO_2 ceramics than pure TiO_2 ceramics, according to the results from surface area measurement.

Table 4.4 Water uptake of PVDF cast film and PVDF/10%wt of Sb doped TiO_2 cast films

Samples	Percentage of Water Uptake
PVDF Cast Film	4.66
PVDF/10%wt of TiO_2	8.74
PVDF/10%wt of 5 mol%Sb-TiO_2	11.20
PVDF/10%wt of 10 mol%Sb-TiO_2	10.60
PVDF/10%wt of 20 mol%Sb-TiO_2	11.68

4.4.2.5 Proton Conductivity Measurement of PVDF-10%wt of Sb Doped TiO_2 Cast Films

The results of resistance and proton conductivity of all membranes at room temperature after soaking in 6M H_2SO_4 aqueous solution were demonstrated in Table 4.5. The proton conductivity value of PVDF/Sb doped TiO_2 films were enhanced by doping antimony into TiO_2 matrix because the doped TiO_2 showed higher specific surface areas, leading to obtain higher water adsorption ability, and the porous surface condition of the TiO_2 ceramic particles was improved by doping antimony. High surface areas and the acidic porous surface condition of the ceramic particles cause easier proton hoping, resulting in an increase of proton conductivity value.

Table 4.5 Resistance and proton conductivity at 25 ° C of PVDF cast film and PVDF/10%wt of Sb doped TiO_2 cast films

Samples	Resistance (Ohms)	Proton Conductivity (S/cm)
PVDF Cast Film	1183.74	9.04×10^{-6}
PVDF/10%wt of TiO_2	813.89	1.92×10^{-5}
PVDF/10%wt of 5 mol%Sb-TiO_2	412.56	3.78×10^{-5}
PVDF/10%wt of 10 mol%Sb-TiO_2	435.88	3.67×10^{-5}
PVDF/10%wt of 20 mol%Sb-TiO_2	421.65	3.77×10^{-5}

4.4.3 PVDF-5 mol% Antimony Modified Titanium Dioxide (5 mol%Sb-TiO_2) Composite Film in Various Amounts of Ceramic Powder

4.4.3.1 SEM/EDX Analysis of PVDF-5 mol%Sb Doped TiO_2 Thin Films

SEM micrograph of the composites containing 10, 20, 30, 40, and 50 wt% ceramic filler which fine powder was dispersed in a PVDF matrix were shown in Figures 4.11. The composites displayed the microstructure of larger agglomeration in PVDF matrix when amount of ceramic increased. However, at higher ceramic content, the flexibilities of composite films were reduced due to the high stiffness of ceramic powder.

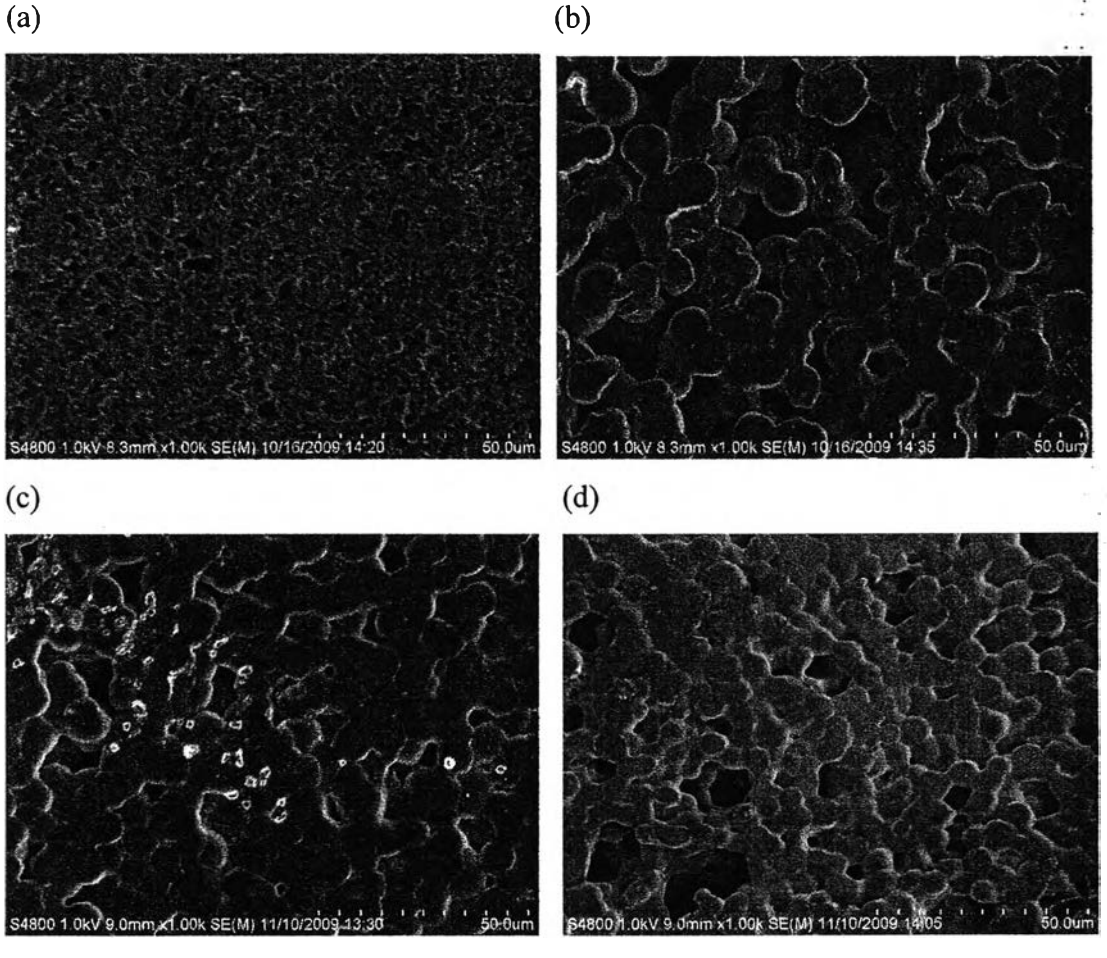

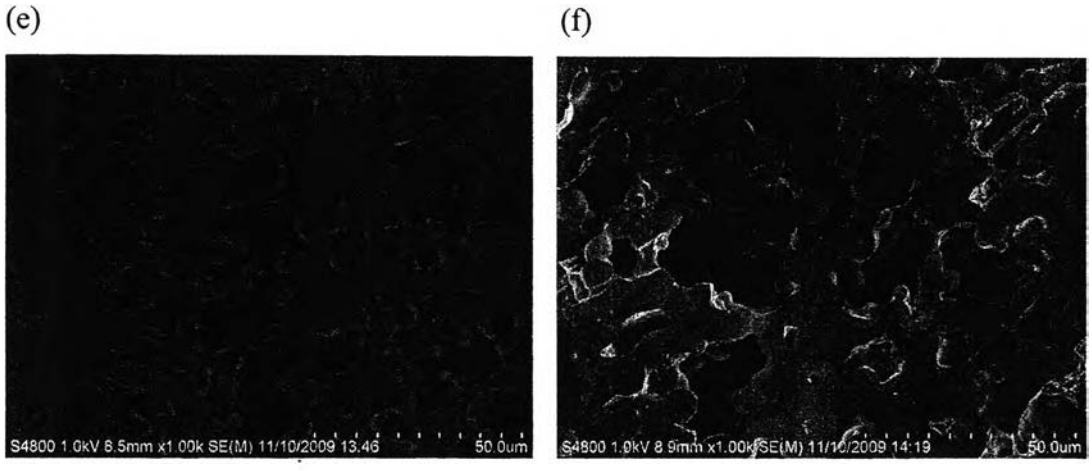

Figure 4.11 SEM images of (a) PVDF cast film, (b) PVDF-10%wt of 5 mol%Sb-TiO_2, (c) PVDF-20%wt of 5 mol%Sb-TiO_2, (d) PVDF-30%wt of 5 mol%Sb-TiO_2, (e) PVDF-40%wt of 5 mol%Sb-TiO_2, (f) PVDF-50%wt of 5 mol%Sb-TiO_2.

In addition, EDX analysis was used to observe the distribution and dispersion of ceramic powder in the PVDF matrix. EDX Sb and Ti-mapping photographs show the homogeneous and uniform distribution of Sb-TiO_2 ceramic in PVDF matrix as presented in Fig. 4.12, 4.13, 4.14, 4.15 and 4.16.

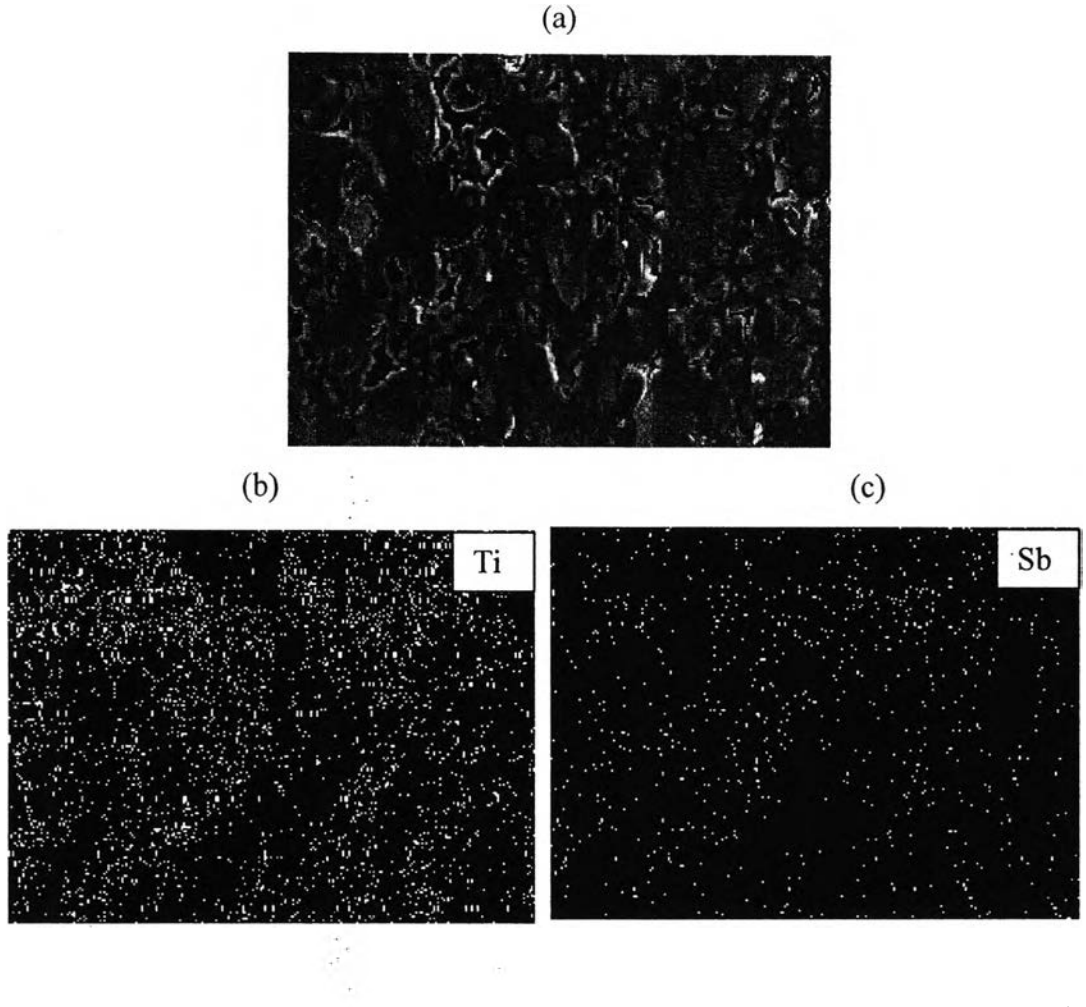

Figure 4.12 (a) SEM image (scale bar = 10 μm), (b) EDX Ti-mapping photograph, (c) EDX Sb-mapping photograph of PVDF-10%wt of 5 mol%Sb-TiO_2.

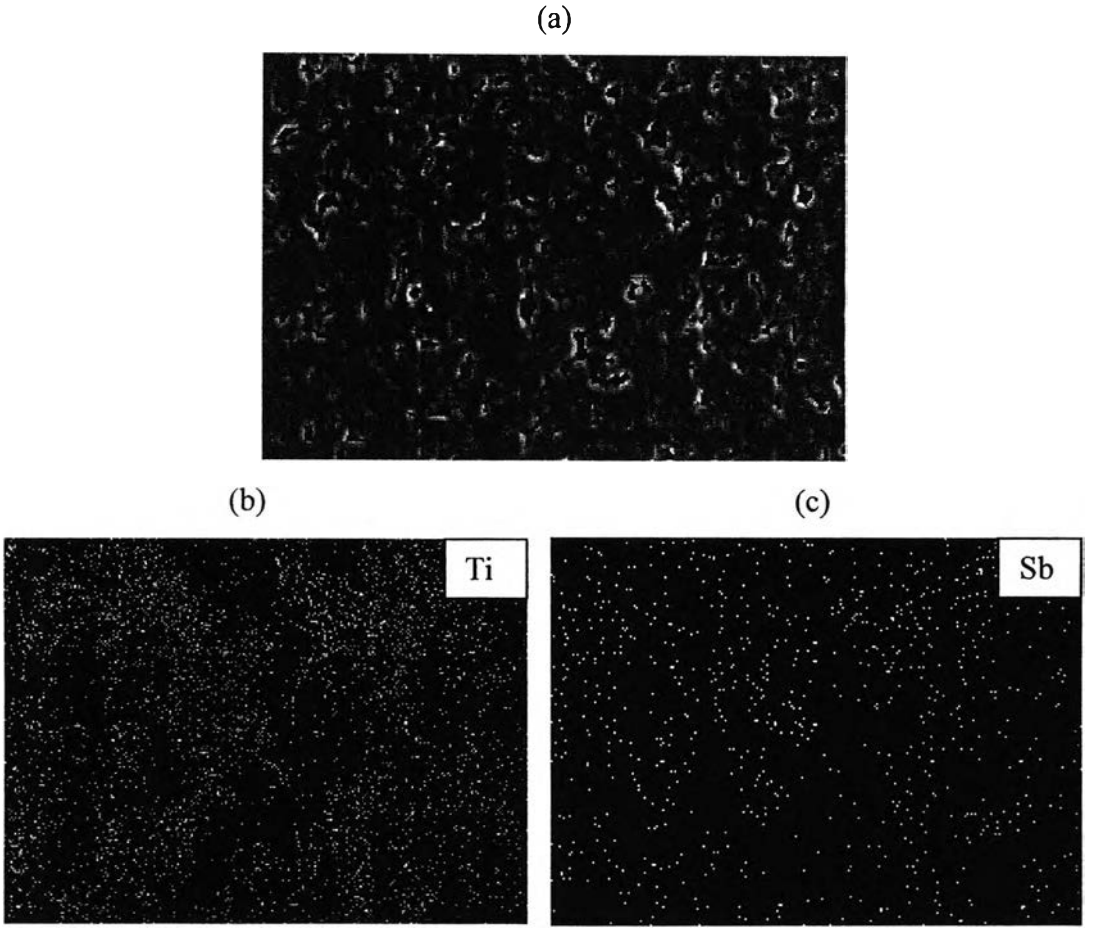

Figure 4.13 (a) SEM image (scale bar = 10 μm), (b) EDX Ti-mapping photograph, (c) EDX Sb-mapping photograph of PVDF-20%wt of 5 mol%Sb-TiO_2.

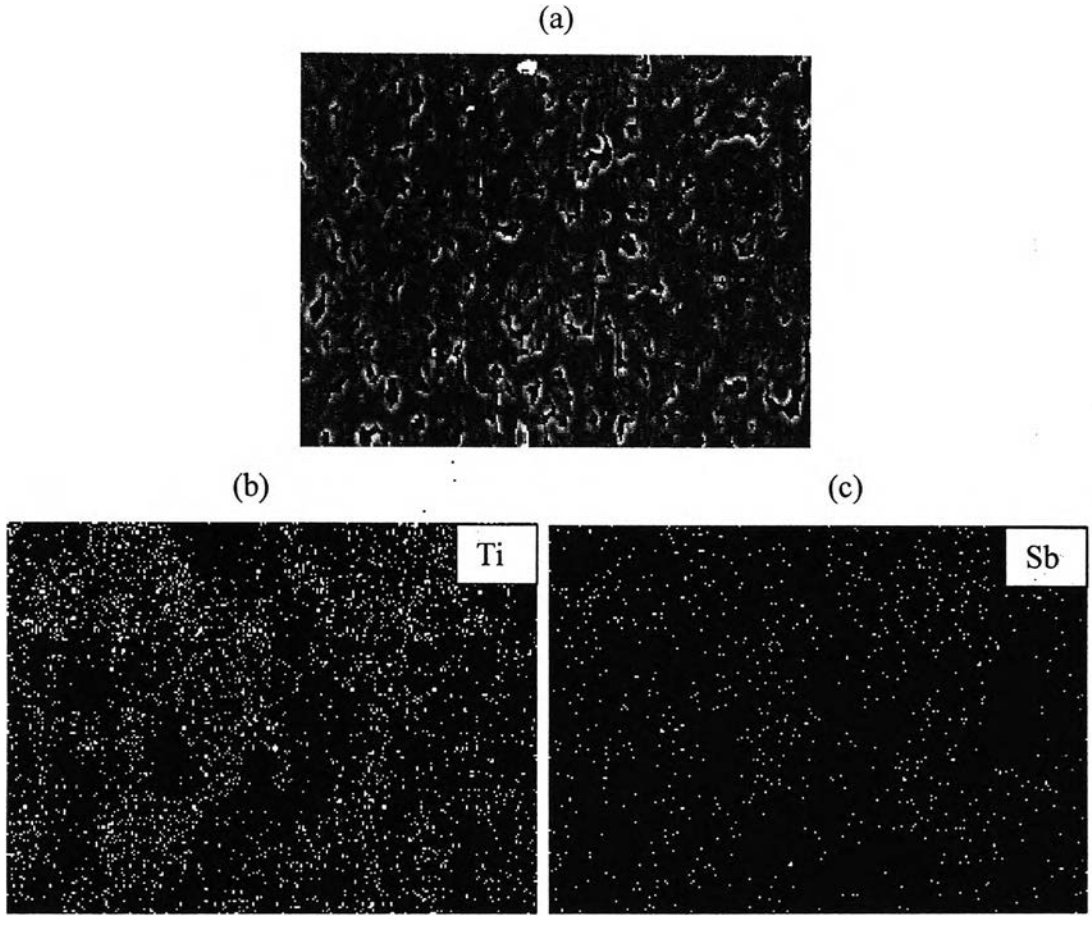

Figure 4.14 (a) SEM image (scale bar = 10 μm), (b) EDX Ti-mapping photograph, (c) EDX Sb-mapping photograph of PVDF-30%wt of 5 mol%Sb-TiO_2.

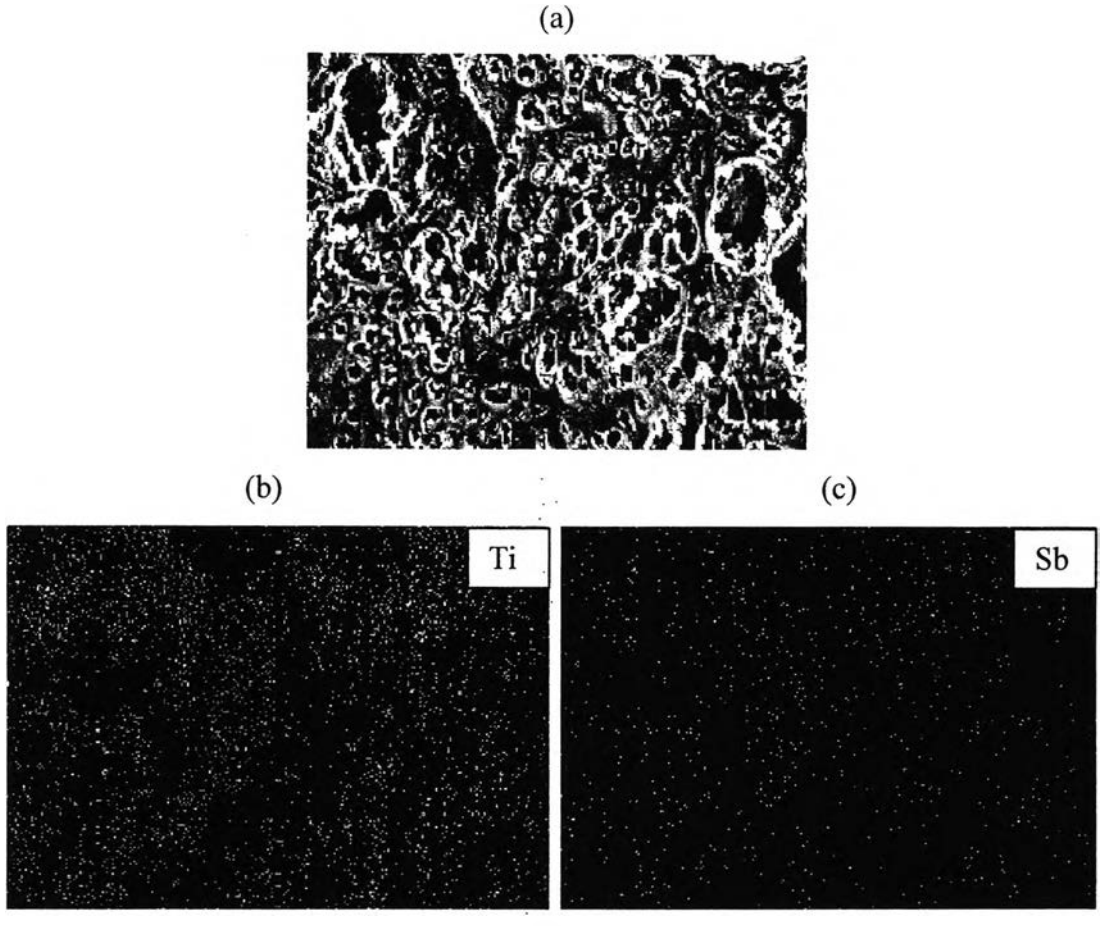

Figure 4.15 (a) SEM image (scale bar = 10 μm), (b) EDX Ti-mapping photograph, (c) EDX Sb-mapping photograph of PVDF-40%wt of 5 mol%Sb-TiO_2.

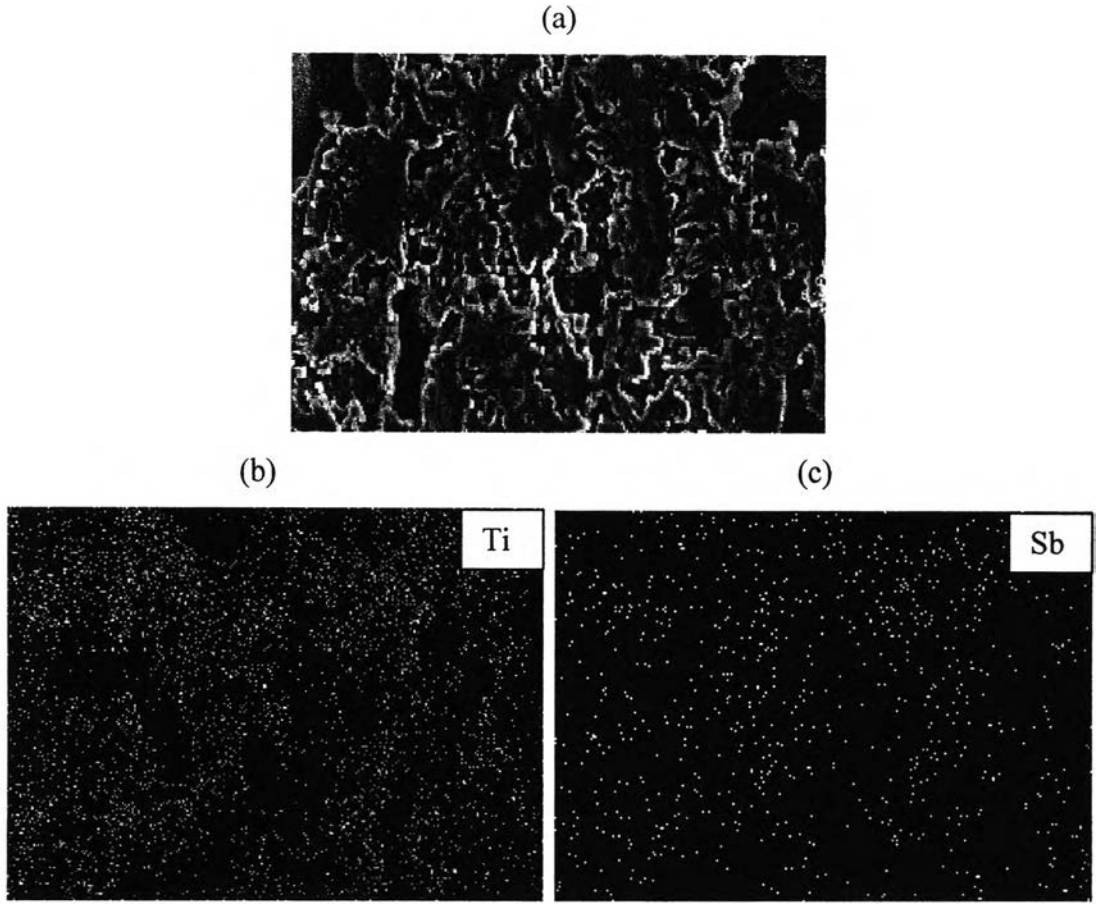

Figure 4.16 (a) SEM image (scale bar = 10 μm), (b) EDX Ti-mapping photograph, (c) EDX Sb-mapping photograph of PVDF-50%wt of 5 mol%Sb-TiO_2.

4.4.3.2 TGA Analysis of PVDF-5 mol%Sb Doped TiO_2 Thin Films

The graphic of weight loss versus temperature for PVDF and PVDF/5 mol%Sb-TiO_2 composite as shown in Figure 4.17. It can be observed that the relative mass decayed at temperature below 150 ° C and another mass loss is at approximately near 400 ° C. The first mass loss indicates the presence of water, while the second one presents the decomposition of PVDF. TGA thermograms showed that the incorporation of 5mol%Sb-TiO_2 ceramic in the PVDF films enhances the higher residue of composite when compared to the pure PVDF.

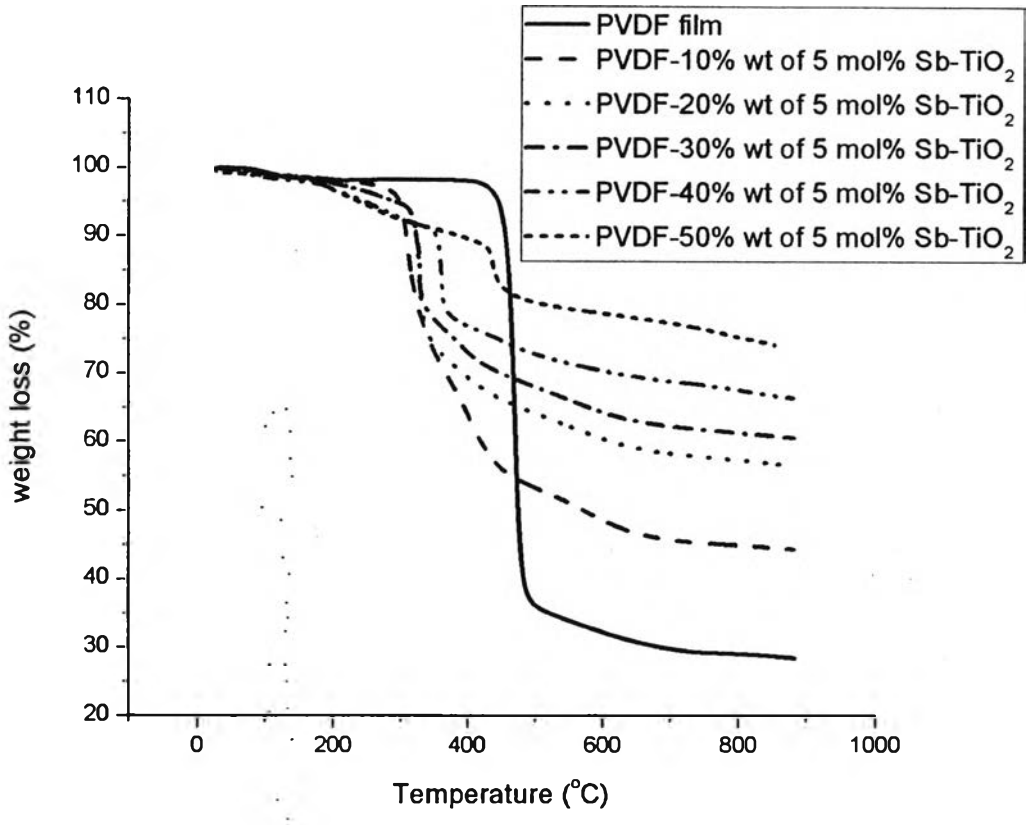

Figure 4.17 TGA thermograms of PVDF cast film and PVDF-5 mol%Sb doped TiO_2 cast films.

4.4.3.3 Mechanical Properties of PVDF/5 mol%Sb-TiO_2 Thin Films

Tensile properties were measured in order to evaluate the stiffness and strength of the thin films. With increasing 5 mol%Sb-TiO_2 contents, the Young's Modulus of composite films increased while the percentage strain at break and the stress at break decreased as it can be seen in the Table 4.6. This may be contributed the high modulus of ceramic and the poor interaction between polymer and ceramic.

Table 4.6 Mechanical properties of PVDF cast film and PVDF/5 mol%Sb-TiO_2 thin films

Samples	Young's Modulus (MPa)	Stress at Break (MPa)	Percentage Strain at Break
PVDF Cast Film	272.42 ± 2.45	24.66 ± 3.38	17.00 ± 1.26
PVDF/10%wt of 5 mol%Sb-TiO_2	432.02 ± 3.35	17.17 ± 3.78	12.75 ± 3.05
PVDF/20%wt of 5 mol%Sb-TiO_2	463.40 ± 3.96	8.10 ± 1.58	9.66 ± 2.49
PVDF/30%wt of 5 mol%Sb-TiO_2	556.78 ± 2.07	7.03 ± 1.33	5.26 ± 1.87
PVDF/40%wt of 5 mol%Sb-TiO_2	633.13 ± 3.19	5.90 ± 1.43	3.04 ± 0.91
PVDF/50%wt of 5 mol%Sb-TiO_2	729.62 ± 2.85	4.87 ± 1.22	1.63 ± 0.45

4.4.3.4 Water Uptake Testing of PVDF-5 mol%Sb-TiO_2 Thin Films

The results of water uptake testing at room temperature exhibit that percentage of water uptake of composite films increased with the 5 mol%Sb-TiO_2 contents because of the hydrophilicity of the ceramics, as shown in Table 4.7. This increase may be due to the high specific surface areas of 5 mol%Sb-TiO_2 ceramics, according to the results from surface area measurement.

Table 4.7 Water uptake of PVDF cast film and PVDF/5 mol%Sb-TiO_2 thin films

Samples	Percentage of Water Uptake
PVDF Cast Film	4.66
PVDF/10%wt of 5 mol%Sb-TiO_2	11.20
PVDF/20%wt of 5 mol%Sb-TiO_2	11.91
PVDF/30%wt of 5 mol%Sb-TiO_2	13.06
PVDF/40%wt of 5 mol%Sb-TiO_2	15.32
PVDF/50%wt of 5 mol%Sb-TiO_2	17.63

4.4.3.5 Proton Conductivity Measurement of PVDF-5 mol%Sb Doped TiO_2 Thin Films

The results of resistance and proton conductivity of all membranes at room temperature after soaking in 6M H_2SO_4 aqueous solution for 24 hours were demonstrated in Table 4.8. The proton conductivity value of composite membranes were enhanced by increasing 5 mol%Sb-TiO_2 particles because this ceramic showed higher specific surface areas, leading to obtain higher water adsorption ability. High surface areas and the acidic porous surface condition of this particles cause easier proton hoping, resulting in an increase of proton conductivity value.

Table 4.8 Resistance and conductivity at 25 °C of PVDF cast film and PVDF/5 mol%Sb-TiO_2 thin films

Samples	Resistance (Ohms)	Proton Conductivity (S/cm)
PVDF Cast Film	1183.74	9.04×10^{-6}
PVDF/10%wt of 5 mol%Sb-TiO_2	412.56	3.78×10^{-5}
PVDF/20%wt of 5 mol%Sb-TiO_2	115.67	2.20×10^{-4}
PVDF/30%wt of 5 mol%Sb-TiO_2	54.17	6.15×10^{-4}
PVDF/40%wt of 5 mol%Sb-TiO_2	20.41	1.63×10^{-3}
PVDF/50%wt of 5 mol%Sb-TiO_2	0.86	4.63×10^{-2}

From all of these results, the optimum %wt of ceramic in PVDF matrix should be 40%wt due to the high percentage of water uptake, high proton conductivity and good flexibility of this film. The temperature dependence of proton conductivity of PVDF film and PVDF/40%wt of 5 mol%Sb-TiO_2 composite were investigated from -40 °C to 140 °C in Figure 4.18. From these graphs, it should be observed that the proton conductivity of PVDF composite increased rapidly (~10^{-4}

S/cm to ~10^{-1} S/cm) in the long range of temperature (-40 °C to 90 °C) before decreased rapidly (~10^{-1} S/cm to ~5×10^{-3} S/cm) in the short range of temperature (90 °C to 140 °C). The behavior of conductivity decreasing above 100 °C suggests the higher dehydration of the membrane with higher temperature. However, the composite film can keep the proton better than pure PVDF film due to the pore structure of ceramic powder. At 90 °C, the proton conductivity for the PVDF/40%wt of 5 mol%Sb-TiO_2 composite film is 0.0856 S/cm, which is the maximum conductivity value.

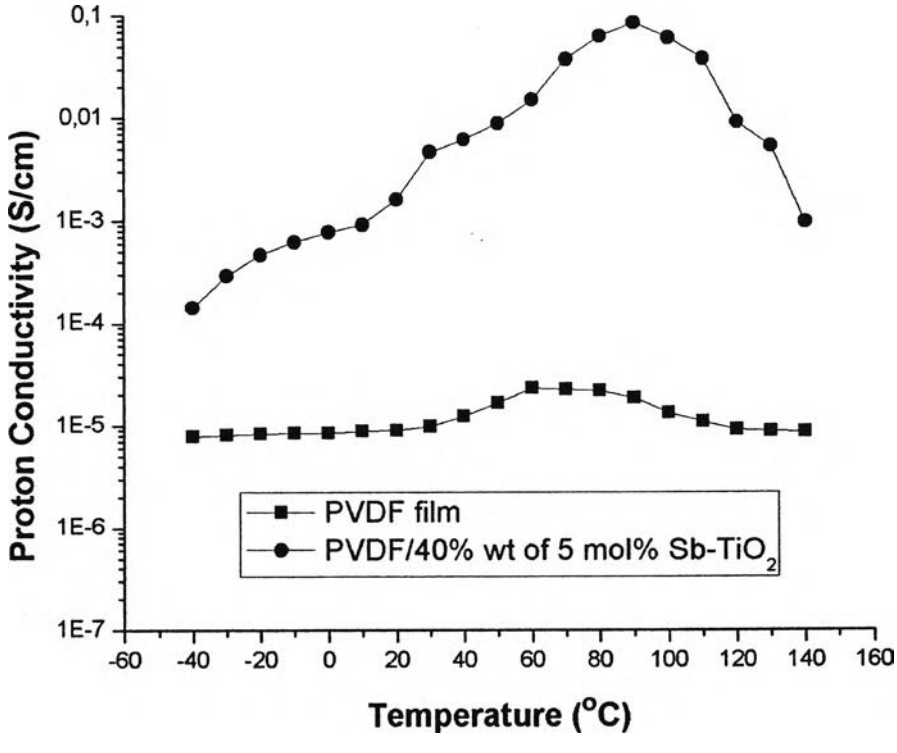

Figure 4.18 The temperature dependence of proton conductivity of PVDF film and PVDF/40%wt of 5 mol%Sb-TiO_2 films.

4.5 Conclusion

The PVDF/5 mol% Sb-TiO_2 composites were successfully fabricated. By doping Sb in TiO_2, the pore structure of ceramic was improved. The high contents of 5 mol% Sb-TiO_2 in the composite show enhancement of a percentage of water uptake

and proton conductivity compared to pure PVDF film. However, more agglomeration of ceramic powder were found in composites at higher 5 mol% Sb-TiO_2 content which made them opaque, stiff and easy to break. The optimum % wt of ceramic in PVDF composite is 40 % wt due to the good flexible film and 3 orders of magnitude higher than the pure PVDF film.

4.6 Acknowledgement

The authors would like to thank Dr. Pitak Laoratanakul and MTEC staffs for useful assistance and instruments for characterizations. The partial funding of research work was provided by Polymer Processing and Polymer Nanomaterials Research Unit, National Science and Technology Development Agency (NSTDA), Thailand and National Center of Excellence for Petroleum, Petrochemicals, and Advanced Materials, Thailand.

4.7 References

[1] M. A. Navarra, S. Materazzi, S. Panero, and B. Scrosati (2003) PVdF-Based Membranes for DMFC Applications, Journal of the Electrochemical Society, 150 (11), A1528-A1532.

[2] P. Moszczynski (2007) Interpenetrating ionomer–polymer networks obtained by the *in situ* polymerization in pores of PVdF sponges as potential membranes in PEMFC applications, Journal of Power Sources, 173, 648–656.

[3] A. Martinelli, M.A. Navarra, A. Matic, and S. Panero (2005) Structure and functionality of PVdF/PAN based, composite proton conducting membranes, Electrochimica Acta, 50, 3992–3997.

[4] Nikhil H. Jalani, Katherine Dunn, and Ravindra Datta (2005) Synthesis and characterization of Nafion®-MO_2 (M = Zr, Si, Ti) nanocomposite membranes for higher temperature PEM fuel cells, Electrochimica Acta, 51, 553–560.

[5] Zhu Bin, Mei Bingchu, Shen Chunhui, and Yuan Runzhang (2006) Study on the electrical and mechanical properties of polyvinylidene fluroide/titanium

silicon carbide composite bipolar plates, Journal of Power Sources, 161, 997–1001.

[6] T. Kuanchaitrakul, S. Chirachanchai and H. Manuspiya (2008) Inorganic mesoporous membrane for potentially used in proton exchange membrane.

[7] M. A. Navarra, S. Panero, and B. Scrosati (2004) A composite proton-conducting membrane based on a poly(vinylidene)fluoride-poly(acrylonitrile), J Solid State Electrochem, 8, 804–808.

[8] Flavio Maron Vichi, Maria Isabel Tejedor-Tejedor, and Marc A. Anderson (2005) Proton conductivity in tungsten and antimony-modified titania ceramics prepared by the sol–gel method, Solid State Ionics, 176, 973–978.

[9] A. Ahmad, J.Thiel, and S.Ismat Shah (2007) Structural effects of niobium and silver doping on titanium dioxide nanoparticles, Journal of Physics: Conference Series 61, 11–15.

[10] Xu, J., Jia, C., Cao, B., Zhang, W.F. (2007) Electrochemical propertied of anatase TiO_2 nanotubes as an anode material for lithium-ion batteries, Electrochimica Acta, 52, 8044-8047.

[11] Lee, J.E., Oh, S.M., and Park, D.W. (2004) Synthesis of nano-sized Al doped TiO_2 powders using thermal plasma. Thin Solid Films, 457, 230-234.

[12] Chen, D., Jiang, Z., Geng, J., Wang, Q., and Yang, D. (2007) Carbon and Nitrogen Co-doped TiO2 with Enhanced Visible-Light Photocatalytic Activity, Ind. Eng. Chem. Res., 46, 2741-2746.

[13] N. Venkatachalam, M. Palanichamy, Banumathi Arabindoo, V. Murugesan (2007) Enhanced photocatalytic degradation of 4-chlorophenol by Zr^{4+} doped nano TiO_2, Journal of Molecular Catalysis A: Chemical 266 158–165.

[14] Amit Chatterjee, Muhammad S. Islam (2008) Fabrication and characterization of TiO_2–epoxy nanocomposite, Materials Science and Engineering A 487, 574–585.

[15] M.T. Colomer (2006) Nanoporous anatase ceramic membranes as fast-proton-conducting materials, Journal of the European Ceramic Society, 26, 1231-1236.